Dual bound states in the continuum enhanced second harmonic generation with transition metal dichalcogenides monolayer

Peilong Hong[1]*, Lei Xu[2]* and Mohsen Rahmani[2]

The emergence of two dimensional (2D) materials has opened new possibilities for exhibiting second harmonic generation (SHG) at the nanoscale, due to their remarkable optical response related to stable excitons at room temperature. However, the ultimate atomic-scale interaction length with light makes the SHG of Transition Metal Dichalcogenides (TMDs) monolayers naturally weak. Here, we propose coupling a monolayer of TMDs with a photonic grating slab that works with doubly resonant bound states in the continuum (BIC). The BIC slabs are designed to exhibit a pair of BICs, resonant with both the fundamental wave (FW) and the second harmonic wave (SHW). Firstly, the spatial mode matching can be fulfilled by tilting FW's incident angle. We theoretically demonstrate that this strategy leads to more than four orders of magnitude enhancement of SHG efficiency than a sole monolayer of TMDs, under a pump light intensity of 0.1 GW/cm². Moreover, we demonstrate that patterning the TMDs monolayer can further enhance the spatial overlap coefficient, which leads to an extra three orders of magnitude enhancement of SHG efficiency. These results demonstrate remarkable possibilities for enhancing SHG with nonlinear 2D materials, opening many opportunities for chip-based light sources, nanolasers, imaging, and biochemical sensing.

Keywords: second harmonic generation; transition metal dichalcogenides; bound state in the continuum; photonic grating slab

Introduction

Two-dimensional (2D) materials consist of a single layer of atoms of crystalline materials. Beyond graphene, the most famous 2D material, over 700 other 2D materials have been recently explored and introduced for a wide range of electrical, mechanical, thermal, and optical applications[1]. For optical applications, monolayers of transition metal dichalcogenides (TMDs) have attracted significant attention due to their direct bandgap, strong luminescence, and small Bohr radii. These characteristics enable a strong excitonic response at room temperature[2,3]. Moreover, TMDs monolayers are inherently noncentrosymmetric, showing very high second-order nonlinear susceptibility[4–9]. However, because of the intrinsic atomic thickness, the conversion efficiency of the second harmonic generation (SHG) with TMDs monolayer is naturally low, bringing their practical applications into the bottleneck. To enhance the SHG

[1]School of Optoelectronic Science and Engineering, University of Electronic Science and Technology of China (UESTC), Chengdu 611731, China; [2]Advanced Optics & Photonics Laboratory, Department of Engineering, School of Science & Technology, Nottingham Trent University, Nottingham NG11 8NS, UK.

*Correspondence: PL Hong, E-mail: plhong@uestc.edu.cn; L Xu, E-mail: lei.xu@ntu.ac.uk

efficiency of TMDs materials, their integration with various resonant nanostructures has appeared as a promising approach. One of the candidates is metallic nanostructure, whose free-electrons can couple with the incoming electromagnetic radiation to generate surface plasmons. Plasmonic nanostructures have been employed to enhance SHG with TMD monolayers[10−12]. However, high ohmic losses and low damage thresholds of plasmonic structures have limited the advances in this direction. Subsequently, dielectric nanostructures with high refractive indices were developed by using materials with low optical losses, and thereby have been used as an alternative platform to enhance SHG of TMDs monolayers[13−17]. Particularly, the recently explored bound state in the continuum (BIC)[18,19] in high-refractive-index materials has emerged as a promising playground for enhancing SHG with 2D nonlinear materials.

A BIC can be understood as a state that coexists with the extended wave but does not radiate into the continuum space. It was initially proposed by von Neumann and Wigner in 1929, and recently has received significant interest in optics for both fundamental and practical reasons[18−24]. The BIC can support extremely high quality factors (theoretically infinite), leading to high confinement of electric field. An ideal BIC does not couple into free space but can be easily overcome by slightly changing structural parameters. It is also called quasi-BIC, thereby offering an unprecedented platform for nanophotonic research and applications. BICs or quasi-BICs have been employed for lasing[25,26], SHG[27,28], third harmonic generation[29], nonlinear exciton-polariton effect[30], nonlinear imaging[31], etc. Recently, BIC has been employed for enhancing SHG via a heterostructured photonic slab. Such a slab was designed to exhibit BIC in the second harmonic wave (SHW), while the fundamental wave (FW) is resonant with a normal photonic bandgap cavity mode[32]. This design has demonstrated an enhanced SHG, compared with a homogeneous bulk nonlinear material[33]. It is worth noting that recent studies have also demonstrated that the BIC can significantly enhance SHG with TMDs monolayer[34,35]. However, these studies have designed BIC to be resonant with FW.

In this work, we propose a dual BICs scheme for enhancing SHG of integrated TMDs monolayer, i.e., matching both FW and SHW with a pair of BICs, concurrently. The BIC pair is achieved in a photonic grating slab and is classified as TE-type BIC (resonant with FW) and TM-type BIC (resonant with SHW). We chose GaP

as the grating material since GaP is of high refractive index and negligible absorption in a broad spectral window covering near-infrared to the visible range. To match the modes spatially, which is crucial for enhancing SHG via the dual BICs scheme, we have considered the following two approaches. The first approach is to tilt the incident angle of FW when a homogeneous TMDs monolayer is placed on top of the grating slab. This strategy allows dual BICs scheme to enhance SHG, significantly. Second, we show that patterning the TMDs monolayer can even further reinforce the spatial overlap coefficient, which leads to extra enhancement of SHG. With these strategies together, we can enhance the system's SHG efficiency up to > 4×10^7 folds compared to a monolayer of TMDs with pump light of intensity 0.1 GW/cm². We believe that our approaches offer new possibilities in practical applications with TMDs and other 2D nonlinear optical materials.

Scheme and theoretical analysis

To generate a pair of BICs, we consider a photonic grating slab as shown in Fig. 1(a). The cell length (lattice constant) is a, the grating strip's width is w, and the thickness of the grating is t. For this nanostructure, there are two kinds of BICs, i.e., the symmetry-protected BICs located at Γ ($K_x = 0$) and the destructive-interference induced BICs at off Γ ($K_x \neq 0$) position[20−22]. Here we consider a pair of symmetry-protected BICs, which are of different polarizations. One is the TE-type BIC with the electric field polarized along y direction, and the other is the TM-type BIC with the magnetic field polarized along y direction.

The differently polarized BICs are explored due to the consideration of the second-order nonlinear susceptibility of the TMDs monolayer, which is[4,9]

$$\chi^{(2)}_{x'x'x'} = -\chi^{(2)}_{x'y'y'} = -\chi^{(2)}_{y'x'y'} = -\chi^{(2)}_{y'y'x'} = \chi^{(2)}, \quad (1)$$

where x' corresponds to the armchair direction of the TMDs monolayer. In this work, we match the FW mode to be resonant with the TE-type BIC, and the SHW mode corresponds to the TM-type BIC. If the crystal axis of TMDs monolayer (x', y', z') is aligned with the grating slab axis (x, y, z), the effective nonlinear susceptibility $\chi^{(2)}_{x'y'y'} = \chi^{(2)}_{xyy}$ of the TMD monolayer plays the key role in the dual BICs scheme. In this situation, the armchair direction of the TMDs monolayer is along the x axis shown in Fig. 1(a). Consequently, $\chi^{(2)}_{xyy}$ plays the key role in the scheme, and effective second-order polarizability is
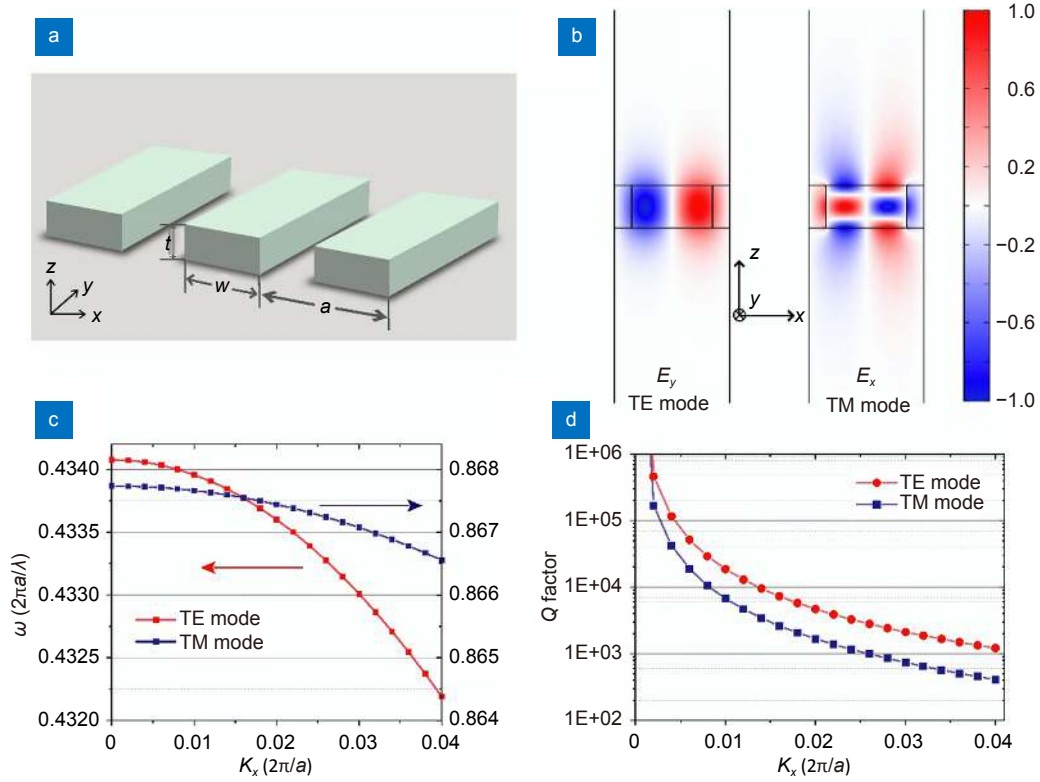
Fig. 1 | Photonic grating slab with a pair of BICs for enhancing SHG. (**a**) Photonic grating slab that contains TE-type and TM-type BICs. (**b**) Spatial distribution of the electric field of TE and TM modes in a unit cell at $K_x = 0$, respectively. (**c**) Band structure of the target TE and TM modes of the photonic grating slab with thickness $t = 0.37 \cdot a$, respectively. (**d**) K_x dependent quality factor of the TE and TM modes shown in (c), respectively.

$$P_x^{(2)}(2\omega, r) = \varepsilon_0 \chi_{xyy}^{(2)} \cdot E_y(\omega, r) \cdot E_y(\omega, r) \ , \qquad (2)$$

where $E_y(\omega, r)$ represents the electric field of the FW.

To make the pair of BICs meet the frequency matching condition for SHG, we fix cell length $a = 677$ nm and the width of grating strip $w = 0.7a$, and scan the thickness t of the grating. We chose GaP as the grating material, which is highly transparent in a broad spectral window from near-infrared to the visible regime. The target wavelength of FW (TE mode) and SHW (TM mode) are 1560 nm and 780 nm, respectively, and the corresponding refractive index of GaP is 3.05 for FW and 3.20 for SHW[36], respectively. The full wave simulation was done with the COMSOL Multiphysics (See Supplemental information Section 1 for details). As an example shown in Fig. 1(c), when thickness t reaches $0.37a$, the frequency of TE-type BIC is half of that of the TM-type BIC state at $K_x \approx 0.16 K_a$, where $K_a = 2\pi/a$. Meanwhile, the quality factor of both TE and TM modes is also obtained, as shown in Fig. 1(d). We see that the quality factor of both TE and TM modes increases as the wave vector K_x decreases, and diverges to infinite at $K_x = 0$. This result confirms that the TE and TM type BICs appear at $K_x = 0$. Note that the diverging quality factor for BICs originates

from that the leakage of the light field from the grating slab to free space is prohibited by the symmetry of the system. As can be seen from Fig. 1(b), the spatial distribution of BICs field in the slab is antisymmetric along x direction, which will eliminate the outcoupling of BICs into free space due to destructive interference. As a result, the light field is confined within the grating slab. Additionally, with K_x close to zero, the BIC is not ideal, but with a limited coupling rate to the free space. Nevertheless, a high quality factor can be reached within a near $K_x = 0$ regime.

To clearly show how the SHG efficiency is enhanced in the dual BICs scheme, let us first recall the temporal coupled mode theory that describes SHG with a pair of resonant modes[32,37−39]. Assuming that A and B are the amplitudes of the FW cavity mode and SHW cavity mode, respectively, and F is the amplitude of incident FW, then their mutual coupling can be described as[38]

$$\frac{\mathrm{d}A}{\mathrm{d}t} = (\mathrm{i}\omega_1 - \gamma_1) \cdot A + g_1 \cdot F - \mathrm{i}\omega_1 \beta_1 A^* B \ , \qquad (3)$$

$$\frac{\mathrm{d}B}{\mathrm{d}t} = (\mathrm{i}\omega_2 - \gamma_2) \cdot B - \mathrm{i}\omega_2 \beta_2 A^2 \ , \qquad (4)$$

here ω_j and γ_j ($j = 1,2$) mean the resonant angular frequency, and the dissipation rate of the cavity mode, respectively. g_j demotes the coupling rate between the cavity mode and freely propagating FW in the continuum, and $|g_1|^2 = 2\gamma_1^{\text{rad}}$ by considering the time reversal and energy conservation according to the temporal coupled mode theory. The last terms of both equations are energy transfer rates between the two cavity modes due to optical nonlinear interaction. The coupling coefficients $\beta_1 = 2\beta_2^{*}{}^{38}$, and β_2 is expressed as

$$\beta_2 = \frac{1}{4} \frac{\int_{\text{TMD}} dr \varepsilon_0 \chi_{xyy}^{(2)} E_{2x}^* E_{1y} E_{1y}}{\int dr \frac{\varepsilon}{2} |\text{E}_1|^2 \sqrt{dr \frac{\varepsilon}{2} |\text{E}_2|^2}} . \tag{5}$$

Now, considering the undepleted pump approximation, the amplitude of SHW cavity modes can be derived as

$$B = \frac{\omega_2 \beta_2}{2\omega - \omega_2 - i\gamma_2} \cdot \frac{g_1^2 F^2}{(\omega - \omega_1 - i\gamma_1)^2} , \tag{6}$$

then, the power of coupling-out SHW can be derived to be

$$P_{2\omega} = 2\gamma_2^{\text{rad}}|B|^2 = \frac{8\gamma_2^{\text{rad}}\omega_2^2|\beta_2|^2}{|2\omega - \omega_2 - i\gamma_2|^2} \cdot \frac{(\gamma_1^{\text{rad}})^2 P_\omega^2}{|\omega - \omega_1 - i\gamma_1|^4} . \tag{7}$$

The relation $P_\omega = |F|^2$ has been used in the derivation, where P_ω denotes the power of incident FW.

By making the FW and SHW resonant with the pair of BICs, i.e., $\omega = \omega_1$, and $2\omega = \omega_2$, we can derive for obtaining the result of dual BICs scheme as

$$\frac{P_{2\omega}}{P_\omega} = \frac{64 |\chi_{xyy}^{(2)}|^2 Q_2 Q_1^2 P_\omega}{\varepsilon_0 \lambda^3 \omega} \cdot \frac{\gamma_2^{\text{rad}}}{\gamma_2} \cdot \frac{(\gamma_1^{\text{rad}})^2}{\gamma_1^2} \cdot Z_{2\omega,\omega}^{\text{TMD}} . \tag{8}$$

In the above equation, $Z_{2\omega,\omega}^{\text{TMD}}$ is the dimensionless overlap coefficient of the paired BICs within the nonlinear 2D material region, expressed as

$$Z_{2\omega,\omega}^{\text{TMD}} = \left| \sqrt{\lambda_1^3} \frac{\int_{\text{TMD}} dr E_{2x}^* E_{1y} E_{1y}}{\int dr \varepsilon_1 |E_1|^2 \sqrt{dr \varepsilon_2 |E_2|^2}} \right|^2 . \tag{9}$$

Note that $\varepsilon_j (j = 1,2)$ is the relative dielectric function of the cavity material for the FW and SHW, respectively. From Eq. (8), we see that besides the well-known incident power P_ω dependence, the SHG efficiency is proportional to the quality factors of the cavity mode Q_j ($j = 1,2$), the ratio of radiative rate to the total dissipation rate of the two cavity modes $\gamma_j^{\text{rad}} / \gamma_j (j = 1,2)$, and the dimen-

sionless overlap coefficient $Z_{2\omega,\omega}^{\text{TMD}}$. In the dual BICs scheme, the quality factors Q_j ($j = 1, 2$) are optimized. There is no other dissipation channel for the cavities in an ideal situation, and $\gamma_j^{\text{rad}} / \gamma_j = 1$ ($j = 1,2$), then $Z_{2\omega,\omega}^{\text{TMD}}$ is the only parameter that needs careful consideration. But in a real situation, absorption and scattering will cause additional dissipation, and then $\gamma_j^{\text{rad}} / \gamma_j$ ($j = 1,2$), together with Q_j and $Z_{2\omega,\omega}^{\text{TMD}}$, will contribute to SHG.

Simulation results and discussions

Now we consider integrating TMDs monolayer onto the photonic grating slab. The selected TMDs monolayer is WS$_2$ with thickness $d_{\text{WS2}} = 0.618$ nm, and its complex refractive index can be extracted from experimental data in the literature[40], which is $\tilde{n}_{\text{TE}} = 3.48 + 0.08i$ for FW (~1560 nm) and $\tilde{n}_{\text{TM}} = 3.85 + 0.20i$ for SHW (~780 nm). A direct way is to place the WS$_2$ monolayer on top of the grating slab as shown in the inset of Fig. 2(a). However, when we look close to the spatial mode structure of the BICs shown in Fig. 1(b), due to the symmetry-protected nature, the pair of BICs are of odd symmetry. As a result, the spatial overlap coefficient $Z_{2\omega,\omega}^{\text{TMD}}$ will be zero at $K_x = 0$, since $E_{2x}(r)$ is odd symmetric while $(E_{1y}(\omega, r))^2$ is even symmetric.

To exploit double BICs for enhancing SHG, the zero spatial overlap case should be circumvented. This can be achieved by selecting quasi-BICs near $K_x = 0$ as the target cavity. Before evaluating the spatial overlap coefficient $Z_{2\omega,\omega}^{\text{TMD}}$ between the paired quasi-BICs upon K_x, we need to find the doubly resonant condition at different K_x. To achieve this goal, we first simulated by scanning K_x and t, and obtained a set of interpolated curves with ω_{TE} v.s. t and ω_{TM} v.s. t at different K_x. With the set of curves, one can numerically get the value t_m that makes $\omega_{\text{TE}} = \omega_{\text{TM}}/2$ at specific K_x, i.e., the doubly resonant condition. This result was further checked in a new full wave simulation with t_m as the parameter. Through this procedure, we can get the structure parameter t_m that makes the pair of quasi-BICs in resonances for enhancing SHG.

With the eigenmode solution through full wave simulation at the doubly resonant condition, we calculate the dimensionless overlap coefficient at different K_x between the TE and TM type quasi-BICs. The result is shown in Fig. 2(a). As can be seen, $Z_{2\omega,\omega}^{\text{TMD}}$ increases quickly when K_x leaves zero point, offering the possibility to enhance SHG in the dual BICs scheme.

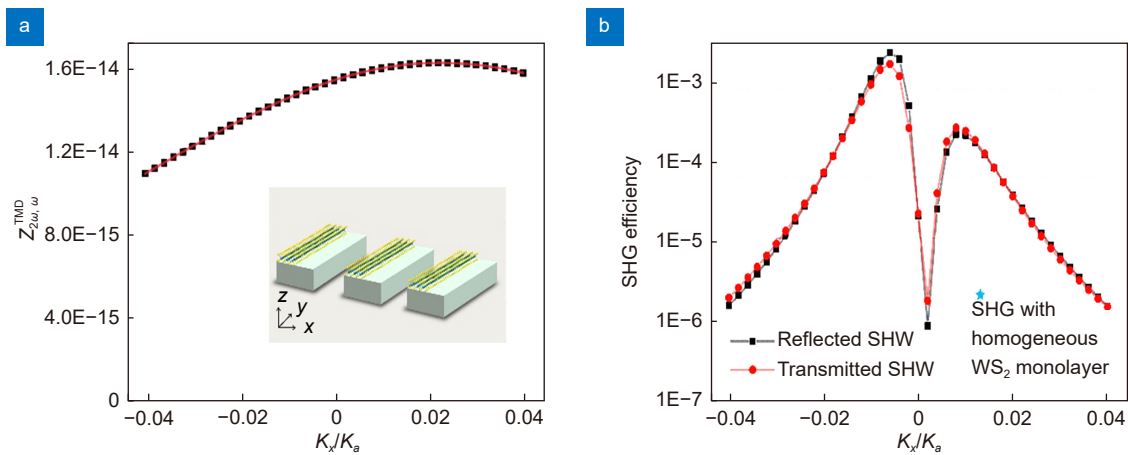To confirm that the dual BICs scheme works in this
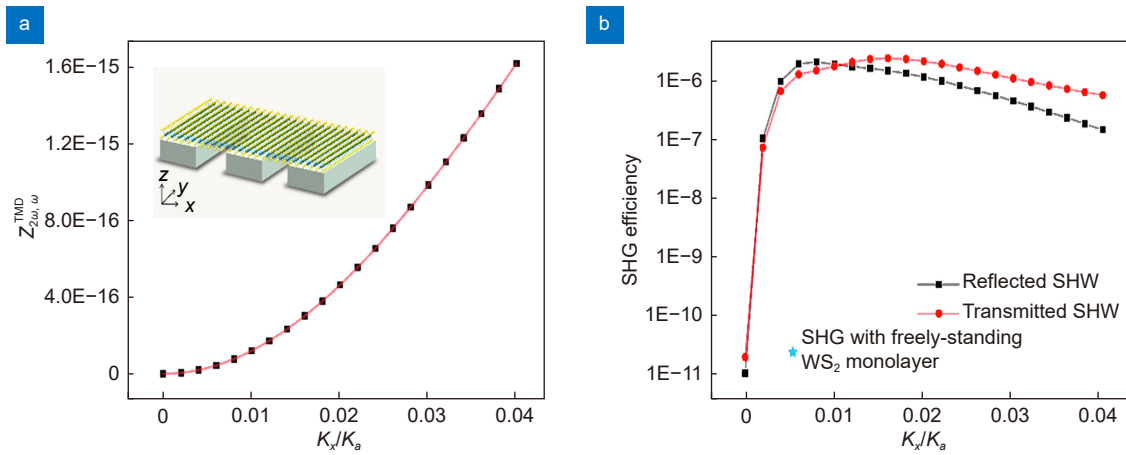
Fig. 2 | Spatial overlap coefficient and SHG efficiency with a homogeneous WS$_2$ on top of the photonic grating slab. (**a**) The K_x dependent spatial overlap coefficient $Z_{2\omega,\omega}^{TMD}$. (**b**) The K_x dependent SHG efficiency monitored at the reflected (top) and transmitted (bottom) side, respectively. The blue star is a reference point for showing the SHG efficiency with a freely-standing WS$_2$ monolayer. The FW is incident from the top side of the grating, and the intensity of FW is set to be 0.1 GW/cm^2.

case, the SHG efficiency $P_{2\omega}/P_\omega$ is obtained by employing a full wave simulation under the undepleted pump approximation. In the simulation, a y-polarized FW is launched from the top side of the grating, and the incident angle θ is related to the wave vector K_x by $K_x = \omega_{TE}/c_0 \sin(\theta)$. The intensity of FW is set to be 0.1 GW/cm^2. We monitor the power of SHW at the top and bottom sides at the same time. Since the structure is mirror-symmetric along x direction, we did a simulation for K_x along the positive direction, expecting that similar results can be obtained with K_x along the negative direction. The simulation result of SHG efficiency is shown in Fig. 2(b). As an example, the electric field distribution of FW and SHW at $K_x = 0.01K_a$ are shown in the Supplemental information Section 2. From the result, we see that the SHG efficiency is quite low at $K_x = 0$, and is at the same order as that of freely standing WS$_2$ monolayer (0.46×10^{-10} with freely standing WS$_2$ with the same excitation intensity). This is expected since light does not couple into the BIC at this condition. However, SHG efficiency increases rapidly when leaving $K_x = 0$ point, and reaches a maximum value $\sim 2 \times 10^{-6}$ ($> 4 \times 10^4$ times of that of freely standing WS$_2$). After that, the SHG efficiency decreases slowly as the incident angle increases to $K_x = 0.04K_a$. This result clearly shows that the dual BICs scheme can work effectively for enhancing SHG with TMDs monolayer.

To fully explore the potential of the dual BICs scheme, we propose to pattern the TMDs monolayer to avoid destructive interference for the dimensionless overlap coefficient shown in Eq. (9). We removed certain parts of the

TMDs monolayer, and in each unit cell, only kept a strip TMDs monolayer of width $0.5w$ on top of the left-half grating strip, as shown in the inset of Fig. 3(a). In this way, $Z_{2\omega,\omega}^{TMD}$ can be enlarged significantly. To confirm this result, we first find the doubly resonant condition at different K_x through the same procedure, as mentioned above. Then, we calculate the spatial overlap coefficient $Z_{2\omega,\omega}^{TMD}$ at different K_x, and the result is shown in Fig. 3(a). Compared with the homogeneous case, $Z_{2\omega,\omega}^{TMD}$ in the patterning case is increased up to ~ 100 times at $K_x = \pm 0.01 K_a$. This high overlap factor is expected to boost the SHG efficiency of WS$_2$ monolayer further.

To check the SHG enhancement, we did a full wave simulation to obtain the SHG efficiency by launching a y-polarized FW of 0.1 GW/cm^2 from the top side. Again, we monitor the power of SHW at both the top and bottom sides of the photonic grating slab. The result of SHG efficiency is shown in Fig. 3(b), and the electric field distribution of FW and SHW at $K_x = 0.01K_a$ are shown in the Supplemental information Section 3. From the result, we see that the SHG efficiency is significantly improved as compared to that with a homogeneous WS$_2$ monolayer. The peak value of SHG efficiency reaches $\sim 2 \times 10^{-3}$ ($> 4 \times 10^7$ times of that of freely standing WS$_2$ monolayer) at a negative incident angle. At a positive incident angle, the enhancement factor is relatively lower, but the peak value still reaches $\sim 2 \times 10^{-4}$. This asymmetric behavior of SHG efficiency upon incident angle is related to mirror symmetry breaking by employing a patterned WS$_2$ monolayer on top of the grating slab (see Supplemental information Section 4). It is precisely the same reason

Fig. 3 | Spatial overlap coefficient and SHG efficiency with a patterned WS$_2$ on top of the photonic grating slab. (**a**) The K_x dependent spatial overlap coefficient $Z_{2\omega,\omega}^{\mathrm{TMD}}$. (**b**) The K_x dependent SHG efficiency monitored at the reflected (top) and transmitted (bottom) side, respectively. The blue star is a reference point for showing the maximum SHG efficiency achieved in the case with homogeneous WS$_2$ monolayer. The FW is incident from the top side of the grating, and the intensity of FW is set to be 0.1 GW/cm^2.

that enables light to be coupled in and out at $K_x = 0$, so that the SHG efficiency is significantly improved at $K_x = 0$, up to ~2×10^{-5}.

The SHG efficiency is limited by the intrinsic absorption of the WS$_2$ monolayer both at the FW mode and the SHW mode. The intrinsic absorption of WS$_2$ leads to the limited value of quality factor Q_j ($j = 1,2$) (~24000 for TE-type BIC, and ~4800 for TM-type BIC in the pattering case). Therefore, the coupling coefficients ratio $\gamma_j^{\mathrm{rad}} / \gamma_j$ ($j = 1,2$) contributes to the total SHG efficiency. To further enhance high SHG efficiency, one can consider spectrum range that is of low absorption, as well as 2D nonlinear materials of low absorption within the interested spectrum range. The finite size of a real 3D device will influence and lower the Q-factor due to the lattice perturbations at the edge breaking the coherence and leading to light scattering into free space. However, numerical investigation shows that a grating of several tens of unit cells can give rise to a high quality factor close to the theoretical one (Supplemental information Section 5). Besides, non-ideal fabrication of the photonic grating in practice could introduce scattering losses, which will affect the performance of BICs. Moreover, it would be interesting to extend the dual BICs scheme to other photonic systems for boosting SHG, and we have summarized the general procedure of designing the dual BICs scheme in Supplemental information Section 6.

It has been found that the polarization of SHG signal can be changed by rotating the crystal orientation of TMDs monolayer[41–43], due to the rich interference phenomena caused by the specific nonlinear susceptibility

tensor of TMDs monolayer. Therefore, the polarization of the SHG signals in the dual BICs scheme should be related to the crystal orientation of the TMDs monolayer. We have investigated this effect by intentionally rotating the orientation of the TMDs monolayer, and the polarization-resolved SHG signal indeed shows an orientation angle dependence (See Supplemental information Section 7 for detailed description and results).

Notably, GaP is a nonlinear optical material, and can exhibit SHG under appropriate condition[44–46], which has been attracting a lot of attention in linear and nonlinear nano photonics recently[47–49]. However, here we consider GaP with its crystal axis corresponding to the axis (x, y, z) in Fig.1 (a), and therefore, due to its specific nonlinear susceptibility, GaP does not exhibit SHG under the incident y-polarized (TE-mode) pump light, and works only as a high refractive index linear material. In a relatively different configuration, i.e., rotating the polarization of pump light to 90 degrees against y axis and scanning the incident angle, GaP can exhibit SHG. In this configuration, the SHG efficiency of GaP is shown in the Supplemental information Section 8, and the maximum efficiency is achieved at a relatively large incident angle (>50 degrees), but is about 2 orders lower than that with homogeneous WS$_2$ monolayer, and 5 orders lower than that with patterned WS$_2$ monolayer.

Conclusions

In conclusion, we propose a dual BICs scheme to enhance SHG with TMDs monolayer. We have shown that a photonic grating slab can be designed to work in the

dual BICs regime, i.e., the FW and SHW are resonant with the TE-type and TM-type BICs, respectively. To fully exploit the advantages of the dual BICs scheme, we have investigated strategies to overcome the limitation of zero overlap coefficient for SHG. With a homogeneous TMDs monolayer on top of the grating, we demonstrated that the spatial overlap coefficient increases as K_x. Subsequently, we managed to optimize SHG by tilting the incident angle of FW, giving rise to $> 4 \times 10^4$ times enhancement at $K_x \approx \pm 0.01 K_a$, as compared to the freestanding situation. Moreover, we showed that patterning the TMDs monolayer can significantly improve the spatial mode overlap coefficient, further boosting the SHG in the dual BICs scheme. We showed that the maximum SHG efficiency at the patterning case is ~10^3 times larger than homogeneous TMDs monolayer at $K_x \approx 0.01 K_a$. And in total, the SHG efficiency reached $> 4 \times 10^7$ times enhancement compared with that with freely standing WS$_2$ monolayer. These results offer new possibilities to enhance SHG in practical applications with TMDs monolayers, which opens new opportunities for nonlinear optics with atomic thin 2D materials.

References

1. Ashton M, Paul J, Sinnott SB, Hennig RG. Topology-scaling identification of layered solids and stable exfoliated 2D materials. *Phys Rev Lett* **118**, 106101 (2017).

2. Schaibley JR, Yu H, Clark G, Rivera P, Ross JS et al. Valleytronics in 2D materials. *Nat Rev Mater* **1**, 16055 (2016).

3. Mak KF, Shan J. Photonics and optoelectronics of 2D semiconductor transition metal dichalcogenides. *Nat Photonics* **10**, 216–226 (2016).

4. Malard LM, Alencar TV, Barboza APM, Mak KF, De Paula AM. Observation of intense second harmonic generation from MoS$_2$ atomic crystals. *Phys Rev B* **87**, 201401 (2013).

5. Liu ML, Wu HB, Liu XM, Wang YR, Lei M et al. Optical properties and applications of SnS$_2$ SAs with different thickness. *Opto-Electron Adv* **4**, 200029 (2021).

6. Kumar N, Najmaei S, Cui QN, Ceballos F, Ajayan PM et al. Second harmonic microscopy of monolayer MoS$_2$. *Phys Rev B* **87**, 161403 (2013).

7. Klein J, Wierzbowski J, Steinhoff A, Florian M, Rösner M et al. Electric-field switchable second-harmonic generation in bilayer MoS$_2$ by inversion symmetry breaking. *Nano Lett* **17**, 392–398 (2017).

8. Autere A, Jussila H, Marini A, Saavedra JRM, Dai YY et al. Optical harmonic generation in monolayer group-VI transition metal dichalcogenides. *Phys Rev B* **98**, 115426 (2018).

9. Janisch C, Wang YX, Ma D, Mehta N, Elías AL et al. Extraordinary second harmonic generation in tungsten disulfide monolayers. *Sci Rep* **4**, 5530 (2014).

10. Li Y, Kang M, Shi JJ, Wu K, Zhang SP et al. Transversely divergent second harmonic generation by surface Plasmon polaritons on single metallic nanowires. *Nano Lett* **17**, 7803–7808

11. Wang Z, Dong ZG, Zhu H, Jin L, Chiu MH et al. Selectively plasmon-enhanced second-harmonic generation from monolayer tungsten diselenide on flexible substrates. *ACS Nano* **12**, 1859–1867 (2018).

12. Shi J, Liang WY, Raja SS, Sang YG, Zhang XQ et al. Plasmonic enhancement and manipulation of optical nonlinearity in monolayer tungsten disulfide. *Laser Photonics Rev* **12**, 1800188 (2018).

13. Day JK, Chung MH, Lee YH, Menon VM. Microcavity enhanced second harmonic generation in 2D MoS$_2$. *Opt Mater Express* **6**, 2360–2365 (2016).

14. Fang CZ, Yang QY, Yuan QC, Gan XT, Zhao JL et al. High-Q resonances governed by the quasi-bound states in the continuum in all-dielectric metasurfaces. *Opto-Electron Adv* **4**, 200030 (2021).

15. Yi F, Ren ML, Reed JC, Zhu H, Hou JC et al. Optomechanical enhancement of doubly resonant 2D optical nonlinearity. *Nano Lett* **16**, 1631–1636 (2016).

16. Fryett TK, Seyler KL, Zheng JJ, Liu CH, Xu XD et al. Silicon photonic crystal cavity enhanced second-harmonic generation from monolayer WSe$_2$. *2D Mater* **4**, 015031 (2016).

17. Chen HT, Corboliou V, Solntsev AS, Choi DY, Vincenti MA et al. Enhanced second-harmonic generation from two-dimensional MoSe$_2$ on a silicon waveguide. *Light Sci Appl* **6**, e17060 (2017).

18. Hsu CW, Zhen B, Stone AD, Joannopoulos JD, Soljačić M. Bound states in the continuum. *Nat Rev Mater* **1**, 16048 (2016).

19. Koshelev K, Bogdanov A, Kivshar Y. Meta-optics and bound states in the continuum. *Sci Bull* **64**, 836–842 (2019).

20. Hsu CW, Zhen B, Lee J, Chua SL, Johnson SG et al. Observation of trapped light within the radiation continuum. *Nature* **499**, 188–191 (2013).

21. Zhen B, Hsu CW, Lu L, Stone AD, Soljačić M. Topological nature of optical bound states in the continuum. *Phys Rev Lett* **113**, 257401 (2014).

22. Doeleman HM, Monticone F, Den Hollander W, Alù A, Koenderink AF. Experimental observation of a polarization vortex at an optical bound state in the continuum. *Nat Photonics* **12**, 397–401 (2018).

23. Jin JC, Yin XF, Ni LF, Soljačić M, Zhen B et al. Topologically enabled ultrahigh-Q guided resonances robust to out-of-plane scattering. *Nature* **574**, 501–504 (2019).

24. Yin XF, Jin JC, Soljačić M, Peng C, Zhen B. Observation of topologically enabled unidirectional guided resonances. *Nature* **580**, 467–471 (2020).

25. Kodigala A, Lepetit T, Gu Q, Bahari B, Fainman Y et al. Lasing action from photonic bound states in continuum. *Nature* **541**, 196–199 (2017).

26. Zhang YW, Chen A, Liu WZ, Hsu CW, Wang B et al. Observation of polarization vortices in momentum space. *Phys Rev Lett* **120**, 186103 (2018).

27. Carletti L, Koshelev K, De Angelis C, Kivshar Y. Giant nonlinear response at the nanoscale driven by bound states in the continuum. *Phys Rev Lett* **121**, 033903 (2018).

28. Koshelev K, Kruk S, Melik-Gaykazyan E, Choi JH, Bogdanov A et al. Subwavelength dielectric resonators for nonlinear nanophotonics. *Science* **367**, 288–292 (2020).

29. Koshelev K, Tang YT, Li K, Choi DY, Li G et al. Nonlinear metasurfaces governed by bound states in the continuum. *ACS Photonics* **6**, 1639–1644 (2019).

30. Kravtsov V, Khestanova E, Benimetskiy FA, Ivanova T, Samusev AK et al. Nonlinear polaritons in a monolayer semiconductor coupled to optical bound states in the continuum. *Light Sci Appl* **9**, 56 (2020).

31. Xu L, Kamali KZ, Huang LJ, Rahmani M, Smirnov A et al. Dynamic nonlinear image tuning through magnetic dipole quasi-BIC ultrathin resonators. *Adv Sci* **6**, 1802119 (2019).

32. Minkov M, Gerace D, Fan SH. Doubly resonant $\chi^{(2)}$ nonlinear photonic crystal cavity based on a bound state in the continuum. *Optica* **6**, 1039–1045 (2019).

33. Wang J, Clementi M, Minkov M, Barone A, Carlin JF et al. Doubly resonant second-harmonic generation of a vortex beam from a bound state in the continuum. *Optica* **7**, 1126–1132 (2020).

34. Wang TC, Zhang SH. Large enhancement of second harmonic generation from transition-metal dichalcogenide monolayer on grating near bound states in the continuum. *Opt Express* **26**, 322–337 (2018).

35. Bernhardt N, Koshelev K, White SJU, Meng KWC, Fröch JE et al. Quasi-BIC resonant enhancement of second-harmonic generation in WS$_2$ monolayers. *Nano Lett* **20**, 5309–5314 (2020).

36. Bond WL. Measurement of the refractive indices of several crystals. *J Appl Phys* **36**, 1674–1677 (1965).

37. Fan SH, Suh W, Joannopoulos JD. Temporal coupled-mode theory for the Fano resonance in optical resonators. *J Opt Soc Am A* **20**, 569–572 (2003).

38. Rodriguez A, Soljačić M, Joannopoulos JD, Johnson SG. $\chi^{(2)}$ and $\chi^{(3)}$ harmonic generation at a critical power in inhomogeneous doubly resonant cavities. *Opt Express* **15**, 7303–7318 (2007).

39. Lin ZN, Liang XD, Lončar M, Johnson SG, Rodriguez AW. Cavity-enhanced second-harmonic generation via nonlinear-overlap optimization. *Optica* **3**, 233–238 (2016).

40. Li YL, Chernikov A, Zhang X, Rigosi A, Hill HM et al. Measurement of the optical dielectric function of monolayer transition-metal dichalcogenides: MoS$_2$, MoSe$_2$, WS$_2$, and WSe$_2$. *Phys Rev B* **90**, 205422 (2014).

41. Maragkakis GM, Psilodimitrakopoulos S, Mouchliadis L, Paradisanos I, Lemonis A et al. Imaging the crystal orientation of 2D transition metal dichalcogenides using polarization-resolved second-harmonic generation. *Opto-Electron Adv* **2**, 190026 (2019).

42. Psilodimitrakopoulos S, Mouchliadis L, Paradisanos I, Kourmoulakis G, Lemonis A et al. Twist angle mapping in layered WS$_2$ by polarization-resolved second harmonic generation. *Sci Rep* **9**, 14285 (2019).

43. Mouchliadis L, Psilodimitrakopoulos S, Maragkakis GM, Demeridou I, Kourmoulakis G et al. Probing valley population imbalance in transition metal dichalcogenides via temperature-dependent second harmonic generation imaging. *npj 2D Mater Appl* **5**, 6 (2021).

44. Sanatinia R, Swillo M, Anand S. Surface second-harmonic generation from vertical gap nanopillars. *Nano Lett* **12**, 820–826 (2012).

45. Cambiasso J, Grinblat G, Li Y, Rakovich A, Cortés E et al. Bridging the gap between dielectric nanophotonics and the visible regime with effectively lossless gallium phosphide antennas. *Nano Lett* **17**, 1219–1225 (2017).

46. Rahmani M, Leo G, Brener I, Zayats AV, Maier SA et al. Nonlinear frequency conversion in optical nanoantennas and metasurfaces: materials evolution and fabrication. *Opto-Electron Adv* **1**, 180021 (2018).

47. Anthur AP, Zhang HZ, Paniagua-Dominguez R, Kalashnikov DA, Ha ST et al. Continuous wave second harmonic generation enabled by quasi-bound-states in the continuum on gallium phosphide metasurfaces. *Nano Lett* **20**, 8745–8751 (2020).

48. Tilmann B, Grinblat G, Berté R, Özcan M, Kunzelmann VF et al. Nanostructured amorphous gallium phosphide on silica for nonlinear and ultrafast nanophotonics. *Nanoscale Horiz* **5**, 1500–1508 (2020).

49. Fedorov VV, Bolshakov A, Sergaeva O, Neplokh V, Markina D et al. Gallium phosphide nanowires in a free-standing, flexible, and semitransparent membrane for large-scale infrared-to-visible light conversion. *ACS Nano* **14**, 10624–10632 (2020).

Acknowledgements

Competing interests

The authors declare no competing financial interests.

Supplementary information

Supplemental material file is included with the manuscript.
https://doi.org/10.29026/oea.2022.200097